Understanding the high performance of nano-sized rutile TiO2 anode for lithium-ion batteries

Pilar Díaz-Carrasco, Angélica Duarte, Alois Kuhn, Flaviano García-Alvarado*

Departamento de Química y Bioquímica, Facultad de Farmacia, Universidad San Pablo-CEU, CEU Universities, Urbanización Montepríncipe, 28668 Boadilla del Monte, Madrid, Spain.

Abstract

The so-called "nanorutile TiO_2 high performance anode material" is somewhat misleading. Below 1.2 V, rutile undergoes an irreversible phase transformation into disordered rock salt-type, c-$LiTiO_2$. During repeated charge-discharge cycling in the 3.0 – 1.0 V range, the cubic structure of $LiTiO_2$ is retained. It is capable of reversibly storing lithium through a solid solution with a noteworthy little volume change as demonstrated by ex situ XRD in samples taken at selected cycles. Interestingly, its good power rate behaviour is not due to fast diffusion of lithium as, in fact, it is strongly inhibited ($D_{Li+} \approx$ 10^{-15} cm^2 s^{-1}). Most of its capacity arises from capacitive processes. At 0.3 mV s^{-1} and higher sweep rates it accounts for more than 50% of total specific capacity, and the capacitive contribution is ca. 90% at 1.5 mV s^{-1}. This work should boost new research on direct synthesis of cubic rock salt-type $LiTiO_2$.

1. Introduction

Amongst transition metal oxides, TiO_2 raised the interest of battery researchers owing to its abundance, low cost and low toxicity, and a safe lithium insertion potential of ca. 1.5 V vs. Li^+/Li. Thus, different TiO_2 polymorphs anatase [1], rutile [2-4], hollandite [5], ramsdellite [6], brookite [7] and TiO_2 (B) [8] have been investigated as prospective negative electrodes for safe Li-ion batteries [9, 10].

Rutile TiO_2, the thermodynamically most stable structure of titanium dioxide, is presently recognised as an alternative to $Li_4Ti_5O_{12}$ (LTO) as the negative electrode in safer Li-ion batteries. However, the path to success of TiO_2 rutile was not straightforward. A very low, almost negligible capacity (< 34 mAh g^{-1})[2, 3], far from the theoretical capacity of 336 mAh g^{-1} was reported for micro-sized TiO_2 rutile. Characteristic for 1-D hosts, lithium insertion in TiO_2 rutile is highly anisotropic, diffusion being several orders of magnitude faster along the *c*-axis channels (10^{-6} cm^2 s^{-1}), than along the *ab* planes [11]. Interestingly, it was found that nanosizing strongly increases both capacity and rate capability of TiO_2 rutile [4, 12-15].

A common characteristic of nanosized rutile TiO_2 is a significant capacity loss after the first discharge, ascribed to an irreversible structural transformation. Discrepancy in literature exists concerning the lithium insertion mechanism. According to [4, 14], during the first discharge, three different voltage regions, with different voltage profiles, were ascribed to different processes: surface storage (2.45 -1.45 V); insertion of Li^+ in an octahedral position in the *ab*-plane of the rutile structure (plateau at 1.4 V); and formation of a nanocomposite of layered hexagonal $LiTiO_2$ and an amorphous phase (1.4-1 V), this nanocomposite being at the origin of the high reversibility and slope-like profile of the

following discharges. Based on potentiostatic intermittent titration technique (PITT) and in situ XRD [13], however, the first two voltage regions were attributed to two consecutive solid solutions corresponding to insertion of lithium in the rutile structure up to x = 0.6, and the third region to a two-phase transformation. Interestingly, the total amount of lithium inserted in the first discharge exceeds the theoretical one for 1 Li/f.u. A combination of *ex-situ* and *operando* total scattering with pair distribution function analysis techniques and transmission electron microscopy [16] showed that the first discharge down to 1 V produces a nanocomposite of layered Li_xTiO_2 with α-$NaFeO_2$ type structure, and a columbite-type related Li_xTiO_2. The structure of the composite is retained upon further cycling following a solid solution mechanism with a volume change as low as 1%. The highly lithiated phase obtained by mechanochemical [13] and chemical [17] lithium insertion of nanorutile resulted in a disordered rock salt-type $LiTiO_2$ and not layered hexagonal $LiTiO_2$ as claimed in other reports [4, 14]. Recently, spindle single crystalline rutile TiO_2 has been shown to keep the rutile structure down to 1 V after 10 cycles [18].

It seems generally accepted that after the first discharge the reduction of particle size contributes to the subsequent high cyclability and rate performance, either because of reduction of mechanical strains [13], owing to decreasing of particle size, or the formation of a special nanocomposite and morphology that better accommodates structural changes [4].

As stated above, nanorutile TiO_2 provides high capacity, excellent capacity retention and power rate, and specific charge capacities of 160 mAh g^{-1} at C/20 rate and 70 mAh g^{-1} at 30 C [4]. Remarkably, a thorough investigation of the relative contribution

of capacitive and faradic processes, in particular at high current densities, has not been reported yet.

As far as synthesis is concerned, Table S1 of Supplemental Information (SI hereafter) shows a selection of different experimental procedures used to obtain nanorutile TiO_2. Available information about morphologies and electrochemical performances have also been listed. Choice of synthesis method and morphology are determining factors for the electrochemical performance of rutile, in which the strong anisotropy of the lithium diffusion coefficient plays a crucial role, as recently demonstrated on rutile TiO_2 epitaxial films with (100) and (001) orientations [19]. Interestingly, McNulty *et al*. [20] reported a first discharge capacity of 608 mAh g^{-1} developed by an inverse opal TiO_2 morphology far beyond the theoretical capacity, due to defect and cation vacancies associated with lithiated oxygen sites. This points to an important role of surface and capacitive processes. However, even in this case the reversible capacity never exceeds that expected for the faradic process corresponding to intercalation of 1 Li/f.u.

In this work, we investigate rutile TiO_2 nanosticks obtained by a two-pot synthesis procedure which is easily scalable and uses cheap reactants. Considering the strong anisotropy in the lithium diffusion [19], and that structural transformation upon lithium insertion reported in different nanorutile TiO_2 samples led to different conclusions, we have investigated the phase transformations upon reaction with lithium. We reveal an extremely interesting phase diagram with two intermediate phases before the end composition $LiTiO_2$ is reached, as deduced from PITT experiments conducted under equilibrium conditions. We aimed to unveil why the performance of nano rutile is outstanding at high current rate, despite the low electronic conductivity and the one-

dimensional character of its diffusion process, which can be expected to be inhibited by defects as in another typical 1-D host for lithium intercalation [21]. Therefore, the electrochemical performance of TiO_2 nanorutile was evaluated as both a capacitive and faradic negative electrode at different current rates. Our study demonstrates that capacitive current contribution masks the true composition of inserted phases. Finally, the lithium diffusion coefficient, D_{Li+}, was determined in pristine rutile TiO_2 nanosticks and the single phase formed after the first cycle.

2. Experimental

TiO_2 nanorutile was synthesised using a two-step process (illustrated in Fig. 1) avoiding the use of unstable or expensive reactants. It consisted in heating a mixture of K_2CO_3 and TiO_2 anatase at 950ºC for 8 h under a 5% H_2/Ar atmosphere to obtain hollandite $K_{0.2}TiO_2$ [22], which was further ball milled for 1 h at 250 rpm to reduce particle size, and was then subjected to strong oxidative/acidic conditions. In a typical experiment 0.4 g of $K_{0.2}TiO_2$ was treated successively with five 1mL-portions of 1:3 HNO_3: HCl mixture for 48 h at 80ºC.

Structural characterisation was carried out by means of X-ray diffraction on a Bruker D8 high-resolution diffractometer equipped with a solid-state position sensitive rapid LynxEye® detector (PSD) using Cu-Kα radiation (λ = 1.5418 Å). Ex situ XRD studies and post-mortem analysis were made on cycled electrodes. Batteries were opened in an argon-filled glovebox and the electrodes were loaded in an airtight sample holder to prevent them from reaction with moisture and air.

All diffraction patterns were analysed and crystal structures determined by the Rietveld method using the FullProf programme [23]. In Rietveld refinements of

nano-sized TiO_2 rutile and related compounds, an anisotropic broadening of diffraction peaks, owing to its acicular morphology, was considered using the spherical harmonics expansion of the crystallite shapes implemented in FullProf. The size-model 21 was selected (Laue class *4/mmm*).

Morphological characterisation of the hollandite precursor and the oxidation product, TiO_2 nanorutile, was made by Scanning Electron Microscopy (SEM) using a JEOL JSM-6400 microscope.

For the electrochemical characterisation, the positive electrode was prepared from a mixture of TiO_2 nanorutile, carbon Super C65 conductive carbon, and PVDF binder in an 80:10:10 weight ratio. Following prolonged stirring, slurries elaborated with NMP as a solvent were cast onto copper foil. Disc electrodes with 12 mm diameter were dried at 80ºC for 24 h under vacuum. A lithium metal disc was used as the negative electrode. Cell assembly was performed in an argon-filled glove box (H_2O and O_2 content < 0.1 ppm) using Whatman GF/D glass fibre as a separator. The electrolyte was 1M $LiPF_6$ in EC:DMC (1:1 vol %). All electrochemical tests were performed in CR2032 coin cells at 25ºC. Galvanostatic discharge-charge experiments were carried out at different current rates. Cyclic voltammetry at sweep rates ranging from 0.009 mV s^{-1} to 1.5 mV s^{-1} were run in the potential range 2.7-1 V to determine the faradic/capacitive contributions at different voltages and current rates. To analyse the nature of the insertion reactions and to determine the compositional range of solid solutions regions, PITT experiments were run at 10 mV steps every 6 h in the 3-1 V voltage range for the first discharge. To investigate the fifth discharge, a cell was cycled four

times at C/20 and left to relax for 24h before running a PITT experiment in the range

2.6-1 V.

Lithium diffusion coefficient was calculated under the condition of semi-

infinite diffusion by [24, 25]:

$$D = \left(\frac{V_M}{Z\,F\,A}\right)^2 \left(\frac{\Delta E}{\Delta x}\right)^2 \left(\frac{1}{m\,A_W\sqrt{2}}\right)^2 \qquad Eq.1$$

In $Eq.1$ V_M is the molar volume, Z the number of electrons per inserted ion, F the

Faraday constant, m the mass of the active material, and A the specific surface area

of the electrode. The latter was determined by BET experiments (Micromeritics

ASAP 2020 analyser). Galvanostatic intermittent titration technique experiments

were run to determine $\left(\frac{\Delta E}{\Delta x}\right)$ at voltage ranges where solid solutions were detected,

and impedance measurements done. A current pulse corresponding to a C/20 rate

was applied for 0.5 h and left to relax until voltage variation was below 2 mV h^{-1}.

Impedance spectroscopy was used to determine the Warburg coefficient

(A_w) and its change upon reaction with lithium. Measurements were performed at

open circuit voltage condition in a three-electrode cell and at several voltages

during the discharge. Li metal discs were allocated at both the counter and the

reference electrodes. Measurements were carried out at room temperature using a

Biologic VMP3 galvanostat-potentiostat with an Electrochemical Impedance

Spectroscopy channel. Equivalent circuit modelling was made using the Z-Fit (EC-

lab$^{®}$ software). A sinusoidal potential perturbation of 10 mV was applied while

measuring impedance variation at room temperature in the frequency range from 3

x 10^5 Hz to 0.1 Hz.

3. Result and discussion

3.1. A new synthetic procedure to nano rutile TiO$_2$ and its electrochemical performance

Step 1 (Fig. 1) produces royal blue K$_{0.2}$TiO$_2$ hollandite by calcination of bulk TiO$_2$ anatase and K$_2$CO$_3$ in a reducing atmosphere. The soft conditions of step 2 (Fig. 1) produced rutile TiO$_2$ nanosticks with a determined related aspect ratio. The aspect ratio (r$_{asp}$) is defined as r$_{asp}$ = L$_{ave}$/W$_{ave}$, L$_{ave}$ being the average length and W$_{ave}$ the average width of the particles [26].
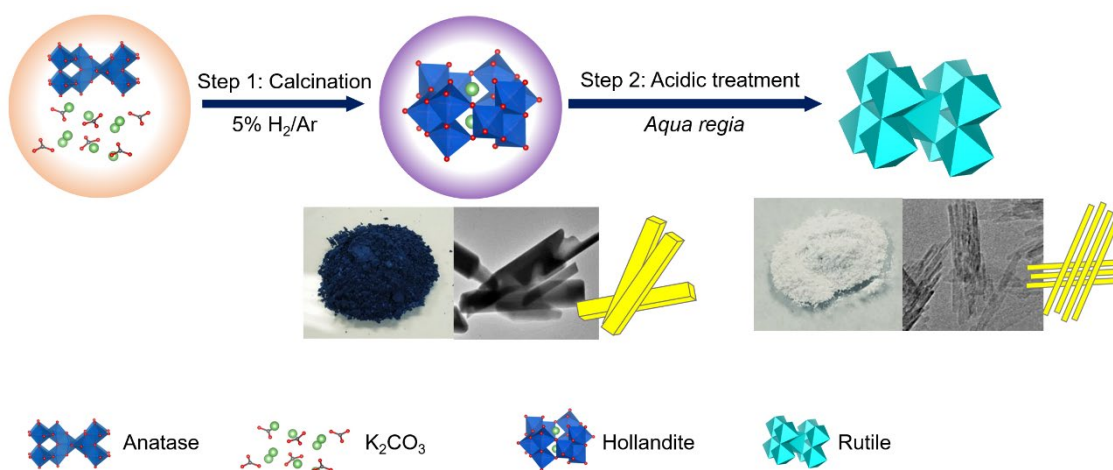

Fig. S1 of SI presents the Rietveld refinement of the X-ray diffraction pattern of as-prepared hollandite K$_{0.2}$TiO$_2$. The lattice parameters with the tetragonal *I*4/*m* space group are refined to a = b = 10.1894 Å and c = 2.9659 Å, consistent with the previously reported values [22, 27, 28]. Hollandite K$_{0.2}$TiO$_2$ shows a well-defined morphology

consisting of crystalline bars as seen in Fig. S2a. The hollandite $K_{0.2}TiO_2$ rods were uniform in length (several microns) and width (~0.45 microns), with the aspect ratio in the range 2.2 - 4.4. To ensure a homogeneous oxidation process, $K_{0.2}TiO_2$ rods were ball milled at 250 rpm for 1 h prior to acidic treatment with 1:3 HNO_3: HCl solution. The result is shown in Fig. S2b of SI. Particles with a different morphology and more homogeneous size distribution and a lower aspect ratio of 2.0 - 2.5 were obtained. X-ray, electron diffraction and X-EDS confirm that the hollandite structure and chemical composition are maintained after the mechanochemical treatment.

Oxidation of nanocrystalline hollandite in an acidic solution of H_2O_2 produces the topotactic extraction of potassium from the hollandite structure as has been previously reported [5, 27]. However, upon prolonged acidic treatment in aqueous 1:3 HNO_3: HCl solution (aqua regia) at 80ºC, potassium extraction is accompanied by a drastic morphological and structural change. Fig. S2c of SI shows the formation of nanosticks 4-5 nm in width and 50-100 nm in length.

Crystal structure analysis revealed that the nanosticks consist of TiO_2 rutile made up of a corner and edge sharing TiO_6 octahedra framework, leaving vacant sites in approximately square tunnels along the [001] crystallographic direction (Fig 2a). Fig. 2b shows the Rietveld refinement of the X-ray diffraction pattern. TiO_2 rutile crystallises tetragonally with space group $P4_2/mnm$, and lattice parameters are refined to $a = b = 4.6044$ Å and $c = 2.9535$ Å. Further crystallographic information of nanorutile TiO_2 is listed in Table S2 of SI. The diffraction pattern is characteristic of a well-ordered material, though anisotropic broadening of (hk0) reflections, in contrast to (00l) reflections, clearly reflects the nanometric nature of TiO_2 rutile exhibiting an anisotropic morphology (Fig. 2c). This is successfully reproduced using the spherical harmonics expansion of the

crystallite shapes as described in the experimental section, yielding excellent Rietveld

R factors R_{wp} = 5.20%, R_p = 3.92% and R_{Bragg} = 1.14%. Fitting the XRD data assuming a

small monoclinic distortion as an alternative description of broadening of reflections in

space group *P*2/*m* (often denoted *P*2/m_{RUT}), as suggested from PDF analysis for as-

prepared rutile [16] and from neutron diffraction for lithiated rutile Li_xTiO_2 (with

intercalation of up to ~0.5 Li per TiO_2) [29], did not provide any improvement (Table

S2). The diffraction profile is therefore best modelled assuming an anisotropic

morphology with the traditional tetragonal *P*4$_2$/*mnm* symmetry. To gain further structural

insight into the nanosized TiO_2, the TEM image in Fig. 2c shows bundles of TiO_2

nanosticks, 5 nm in width and 50 nm in length, with the aspect ratio in the range 10 - 15.

However much longer crystals can be found (See Fig. S2c). The distance of the nearest-

neighbour layers in the HRTEM image (Fig. 2d) is measured as ca. 0.33 nm across and

ca. 0.30 nm along the nanorod, consistent with the interplanar spacings of (110) and (001)

planes for the TiO_2 rutile structure. Therefore, the longer dimension of the nanorod is

along the *c*-axis, which corresponds to the 1-D tunnel along which lithium storage and

diffusion mainly takes place [11].
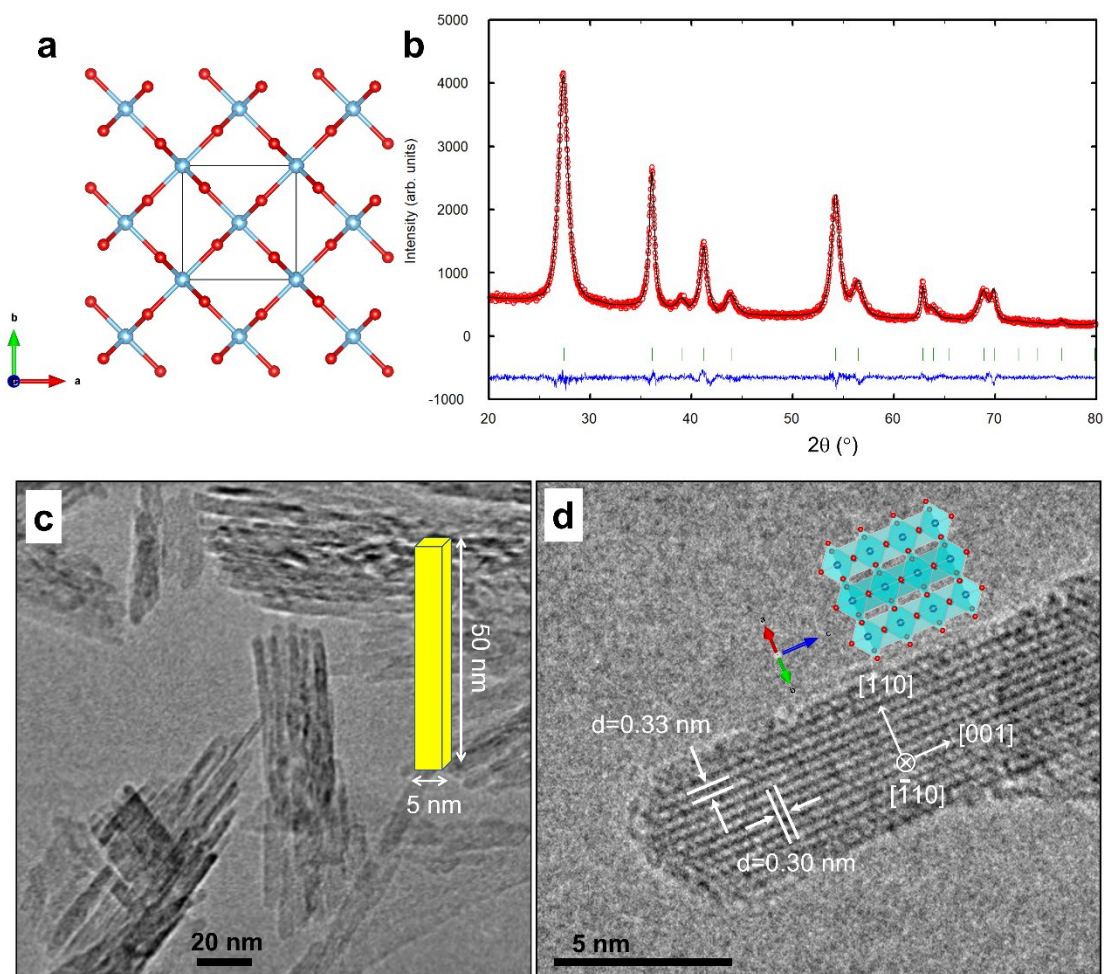
Figure 2: Structural properties of rutile TiO_2 nanosticks. **a)** Crystal structure viewed from the [001] crystallographic direction, Ti: blue spheres, O: red spheres; **b)** Rietveld refinement based on powder XRD; **c)** TEM image of TiO_2 nanorod bundles; **d)** Magnified TEM image of a TiO_2 nanorod along the [-110] zone axis together with its structural model.

The new synthetic path to TiO_2 with rutile structure provided a nanostick morphology. Similar morphology can be also obtained by lower temperature routes such as hydrothermal or hydrolysis procedures, but from more expensive and unstable reagents

such as Ti isopropoxide [16, 30] or $TiCl_4$ [13, 17]. We present an electrochemical characterisation of this TiO_2 nanorutile before deepening the insight into the origin of its high performance.

Fig. 3a shows a typical voltage profile in the OCV-1 V range of the first two discharge-charge cycles and cycle no. 50 of nanorutile TiO_2 in a lithium half-cell under a current of 17 mA g^{-1} (the current to insert 1 Li in 20 hours, C/20). A significant irreversible capacity loss ($\sim$ 30%) occurs after the first discharge, which is a typical behaviour for nanorutile TiO_2 with similar morphologies. For instance, commercial nanorutile TiO_2 [4] shows 40% loss, and previous reports on nanosticks [13] present a 35% loss of initial capacity. Coulombic efficiency at C/20 is high after the first cycle (Fig. 3b). Remarkably, our nano rutile develops a higher capacity not only in the first cycle, above 385 mAh g^{-1}, but also upon cycling when compared to many of the previous reports (see Table S1 and references therein).

The first discharge capacity exceeds that expected for the insertion of 1 Li/f.u (336 mAh g^{-1}), and the high reversible discharge capacity of 230 mAh g^{-1} after the first cycle remains at 180 mAh g^{-1} after 50 cycles. In addition, the TiO_2 nanosticks show an excellent power rate (Fig S3 of SI), exhibiting stable 175 mAh g^{-1} at C/2 after 300 cycles and more than 150 mAh g^{-1} at 2C. These values are among the best reported for rutile TiO_2 for which capacities of 160-200 mAh g^{-1} were observed after 50 cycles [4, 16, 18] and are compared with the rate behavior of other high performant nanorutiles in Table S1.
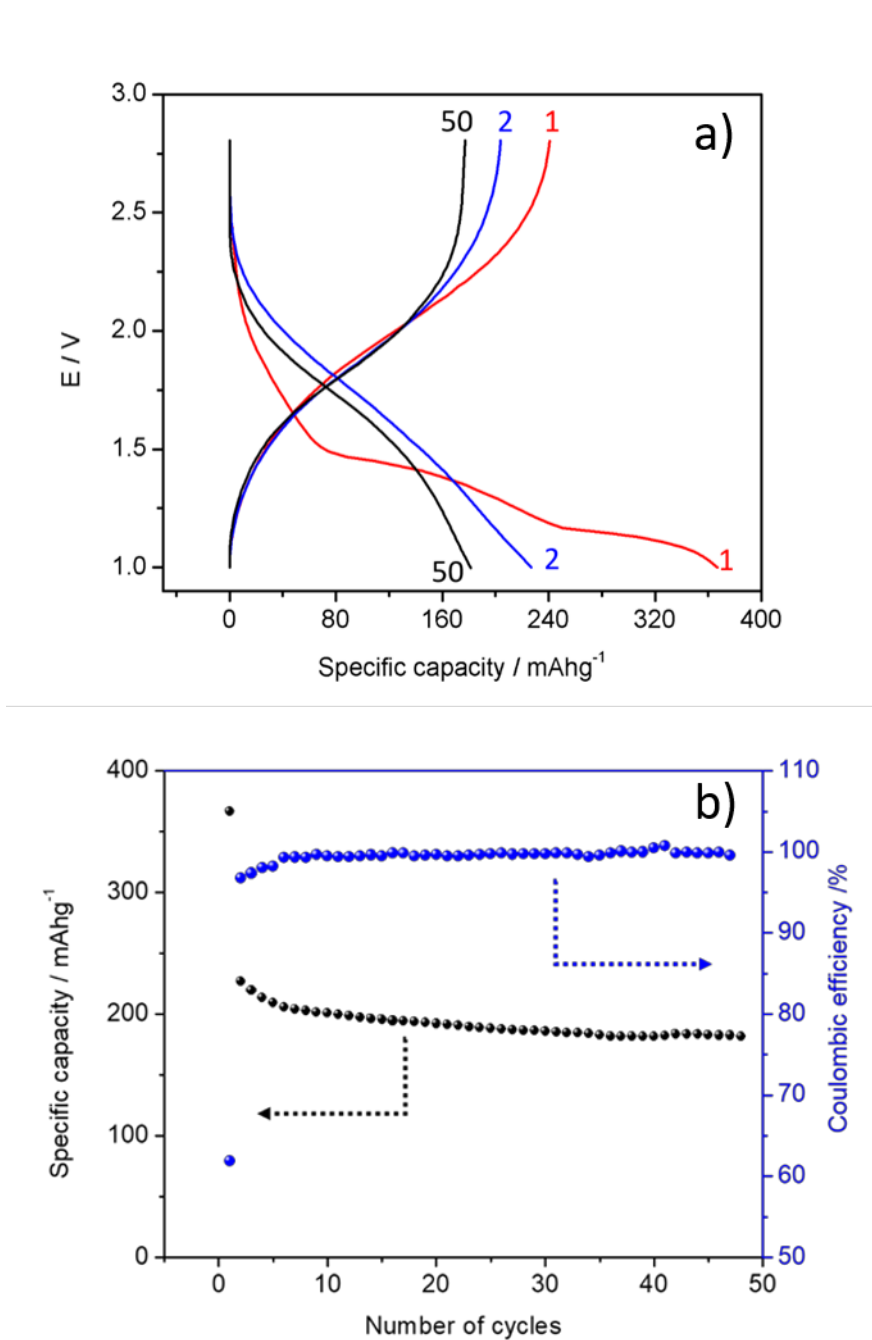
Figure 3: a) Discharge-charge cycling behaviour of rutile TiO_2 nanosticks at C/20

between OCV and 1 V. For sake of clarity, only cycles 1, 2 and 50 are shown; **b)** Variation

of specific capacity and coulombic efficiency upon cycling.

Although different TiO_2 nanorutiles show a similar general electrochemical behaviour, the following important characteristics concerning the reaction of nanosized TiO_2 with lithium are worth being clarified: i) the apparent excess of lithium uptake in the first discharge; ii) the processes taking place during the first discharge and the nature of phases formed at high lithium content, still under dispute, as the dominant factor of subsequent high cyclability; iii) the good performance at high current rate despite the poor transport properties and iv) contribution of capacitive and faradic processes to the total capacity at different current rates.

To address these characteristics, we have investigated the first discharge, performing PITT experiments under almost equilibrium conditions, but scanning the voltage window with narrow potential steps and longer relaxation times at individual potentials than in previous reports [13] in order to avoid the broadening and coalescence of peaks [31], and hence loss of valuable information in complex systems. On the other hand, we have determined the variation of lithium diffusion coefficient between slightly lithiated TiO_2 rutile and the product obtained after the 4th charge, i.e. once capacity is stabilised, and hence assuming that any irreversible structural transformation is completed. In addition, we have investigated the contribution of capacitive processes at different current rates to the specific capacity.

3.2. A phase diagram of the Li-nanorutile TiO_2 system

The differences between the first and following discharges need to be understood, because SEI formation has been observed to form on the surface of TiO_2 at 0.8 V [32], lower than the investigated voltage range, 2.75-1 V. Thus, structural changes in TiO_2 and

their contribution to capacity need to be considered to address the origin of the extra capacity. For this, we present a detailed study of the first discharge.

Fig. 4a shows the variation of voltage during the first discharge down to 1 V together with the relaxation of current at each voltage step of the potentiostatic scan. The different voltage regions are labelled as I, II, II′, III, III′ and IV, and delimited with vertical bars by considering not only the different voltage profile, but also the current relaxation at each voltage step (see Fig S4 of SI for more details). In region I (labelled with C for capacitive in Fig. 4a), current decays very fast and reaches almost zero without any relaxation profile (Fig S4a) characteristic of either mass diffusion (solid solution) or growing of second phases in a biphasic transformation (Fig S4a). This indicates that in this first region a non-faradic process takes place, in agreement with [4], and corresponds to capacitive Li surface storage (0.15 moles of Li). For a better analysis of the Li-TiO_2 phase diagram, the composition axis *"x in Li_xTiO_2"* of Fig. 4a has been re-scaled taking into account the amount of current passed when crossing region I (equivalent to 0.2 moles of Li). Thus, a more reliable estimation of lithium inserted in TiO_2 related to faradic processes can be immediately visualised in that figure. In region II, current relaxation curves (Fig. S4b) indicate the occurrence of a faradic process as lithium diffuses fast into the solid and, therefore, is ascribed to the formation of a narrow solid solution (labelled SS in Fig. 4) with a composition range TiO_2-$Li_{0.19}TiO_2$. In region II′, current relaxation (Fig S4c) points to a more limited kinetics as it does not reach zero as fast as in region II.

On the other hand, the relaxation profile seems to be slightly different at both sides of the current maxima centered at x = 0.3 (Fig S4b). In this region, current decreases in each voltage step in the ascending part of the peak indicating that lithium diffusion in the new phase formed, $Li_{0.4}TiO_2$, is limited, as previously observed for other systems [33].

For compositions $Li_{0.4}TiO_2$-$Li_{0.65}TiO_2$, current relaxation (Fig S4d) points to a single-phase region (III), whereas another biphasic region (III′) is crossed from x = 0.62 to 1.0 (Fig S4e). In region III′ the developed peak is not symmetric, and the anomalous behaviour of current relaxation is clearly far from $t^{-1/2}$ power law, and a different relaxation trend is observed at both sides of the │ I │$_{max}$, characteristic of a biphasic region in the corresponding voltage range [34]. Considering that current at each voltage step remains constant in the ascending part of the peak, we concluded that the two-phase transformation is kinetically limited due to the displacement rate of the interphase zone [33]. Finally, at lower voltages, the current relaxation (Fig. S4f) seems to point to a new solid solution upper compositional limit of which seems to be higher than 1.175 Li/f.u. Again, lithium seems to be intercalated beyond the theoretical limit. However, a more detailed analysis unveils that in the 1.12 -1.0 V range there are two different domains. These are separated by the dashed line depicted in the enlarged view of that voltage region (Fig. 4b). The left domain corresponds to the region labelled IV in Fig 4a. Current reaches the same minimum (see horizontal blue dashed line) in the consecutive voltage steps, and relaxation approaches $t^{-1/2}$ power law. In the right domain the current behaviour is characteristic of a two-phase region with a limited diffusion in the new phase [33] (as in region II′) because the current decreases during each potential step, approaching a $t^{-1/2}$ power law, but it increases from one step to the next (horizontal dashed golden line in Fig 4b). The end of this two-phase region is not detected in the present PITT measurement. The upper limit of the narrow solid solution of region IV has been estimated from the time corresponding to the change of one to the other mentioned current relaxation behaviour. It has been graphically depicted in Fig. 4b by the crossing of the two horizontal dashed straight lines, one of each domain. Thus, region IV corresponds to a very narrow

solid solution $Li_{1.0}TiO_2$-$Li_{1.05}TiO_2$. Hence, this single-phase domain is considered as almost a stochiometric phase with composition $LiTiO_2$.
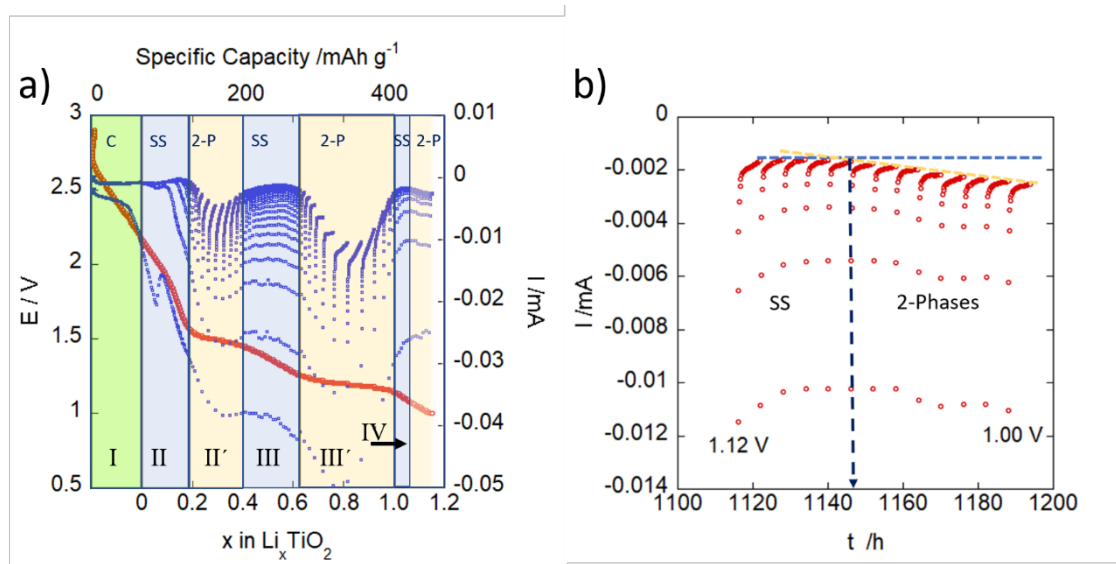

Figure 4: a) Voltage-composition plot of the first discharge recorded under equilibrium conditions using PITT and variation of current in each consecutive voltage step; **b)** Relaxation of current with time at the end of the first discharge in the 1.10-1.0 V range (~ x = 1.05 in Li_xTiO_2).

Our PITT proves that, besides a capacitive process taking place in the 3 (OCV) - 2.15 V range, nanorutile forms two solid solutions, the first one TiO_2-$Li_{0.19}TiO_2$ between 2.15 and 1.55 V (region II in Fig 4) and the second $Li_{0.4}TiO_2$-$Li_{0.62}TiO_2$ between 1.45 y 1.24 (region III in Fig. 4) involving ~0.22 additional lithium ions. They are separated by a wide two-phase region (II′ in Fig. 4) involving 0.2 Li. The formation of solid solution III, at an average voltage of 1.35 V, and the two-phase region at 1.48 V are not clearly identified under constant current and explains the pseudo-plateau observed for similar

compositions in previous reports [4, 13]. More accurate data, collected under equilibrium
conditions at very slow scan rates and long relaxation times for each voltage step, allowed
us to unveil the nature of processes occurring upon reaction with lithium; thus, the true
composition of the two solid solutions and the fully inserted phase at 1.0 V.

From ex situ XRD collected from electrodes discharged to 1.4 V under
galvanostatic conditions (corresponding to formation of $Li_{0.4}TiO_2$ in region III and
recharged to 3.0 V (Fig. 5a), it is evident that insertion/deinsertion of lithium occurs with
retention of the rutile structure, as the Bragg reflections of TiO_2 rutile remain nearly
unchanged, suggestive of nearly unchanged cell parameters. In our refinements (Fig. S5
and S6 of SI) there was no need to consider the slight monoclinic distortion ($P2/m_{RUT}$)
from the tetragonality of rutile as proposed by Christensen *et al*. [16], and XRD profiles
of Li_xTiO_2 rutile were well reproduced assuming anisotropic broadening of diffraction
peaks owing to its acicular morphology. The results agree with previous reports which
proposed that for low lithium contents, the structure of rutile is kept due to the solid
solution nature of the lithiated phase [4, 13], This behaviour is explained in terms of the
reversible insertion of Li^+ into the vacant tunnel sites of rutile TiO_2 [35, 36]. Figs. S7-S10
of SI show the Rietveld refinement patterns of these samples for cycles 4 and 5, and the
corresponding main crystallographic results are given in Table S3 of SI. The rutile
structure is well kept upon cycling in this voltage region, as deduced from the XRD
patterns taken from electrodes discharged down to 1.4 V and charged up to 3.0 V in
successive cycles.
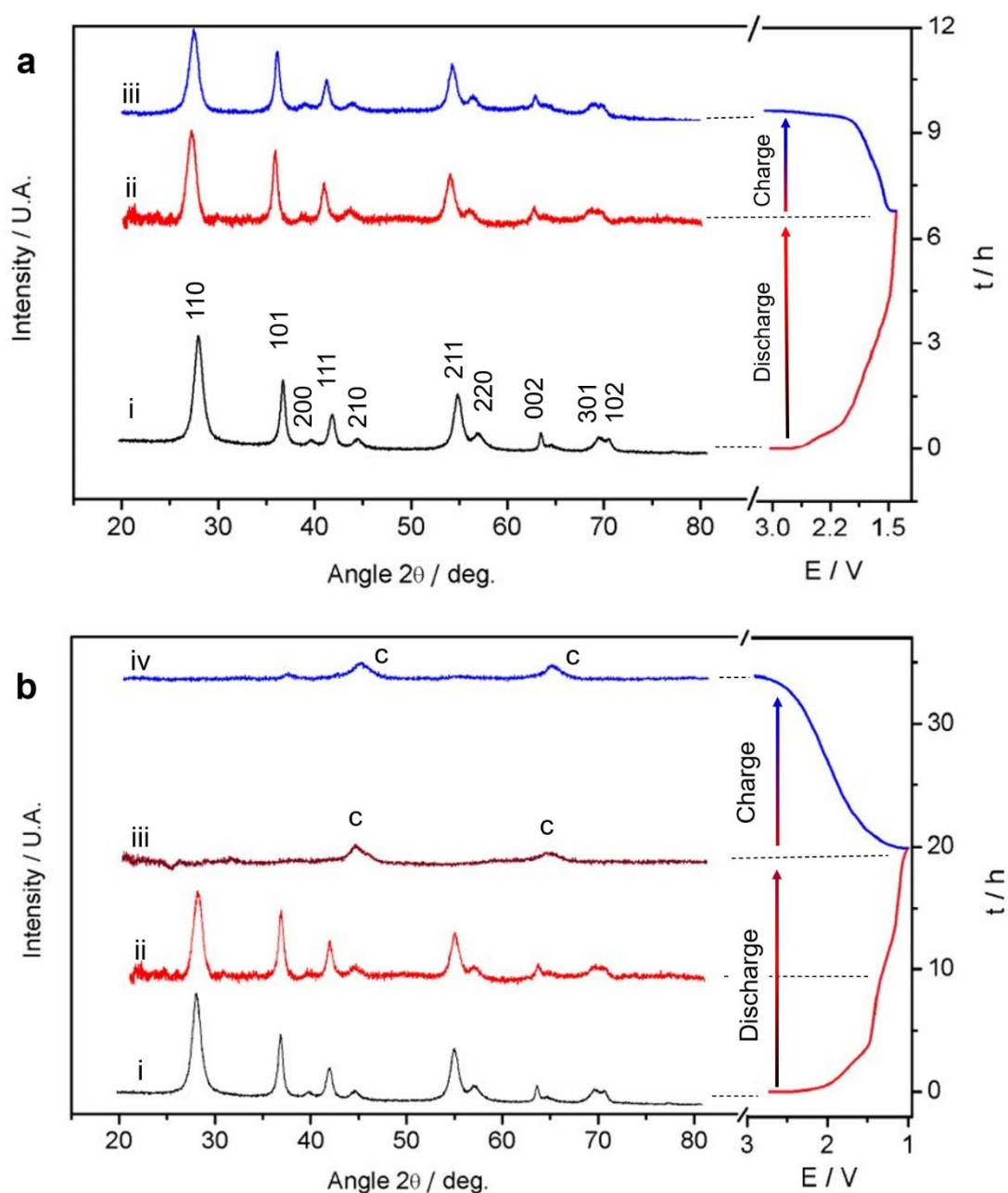
Figure 5: Ex situ XRD patterns of a rutile TiO_2 electrode during the first discharge-charge cycle. **a)** pristine TiO_2 (i), discharged to 1.4 V (ii) and charged to 3.0 V (iii); **b)** pristine TiO_2 (i), discharged to 1.4 V (ii) and 1.0 V (iii) and charged to 3.0 V (iv).

After solid solution III with x = 0.62 Li/f.u, a new phase starts to grow during an irreversible transformation (region III′) and seems to be completed in region IV reaching

the composition $LiTiO_2$ (Fig. 4a). On the other hand, nominal compositions with x > 1,

may be ascribed to the two-phase domain observed at ~1 V (Fig. 4).

When a cell is discharged to lower 1.0 V (corresponding to the formation of

$LiTiO_2$, in region IV, Fig 4a), the disappearance of the original TiO_2 rutile reflections is

evidenced from ex situ XRD (shown in Fig. 5b), and the appearance of new reflections

(labelled with "c"), indicating that a two-phase transformation took place. This process

corresponds to the domain labelled with III' in Fig. 4a, and after its completion phase III

is converted into phase IV. Rietveld refinement based on the ex-situ XRD data of TiO_2

rutile discharged to 1.0 V suggests cubic symmetry with a = 4.104 Å (Table S4 of SI).

Interestingly, the reflections of the cubic phase remain nearly unchanged in peak position

and intensity profiles after charging the cell to 3.0 V, suggesting little changes in lattice

parameters (Fig. 5b and Table S4). It is noteworthy that the formation of an electroactive

cubic $LiTiO_2$ phase, c-$LiTiO_2$ hereafter, with disordered rocksalt structure (a = 4.140 Å,

V = 70.96 Å^3) has been achieved with a more severe reductive process by means of

mechanical grinding of metallic lithium with commercial TiO_2 rutile nanopowder [13].

Interestingly, the role of the synthesis procedure is still to be unveiled inasmuch as the

electrochemically synthesized c-$LiTiO_2$ is a high performance anode whereas the

mechanochemically prepared sample only showed a small capacity [13].

To gain more insight into the cyclability of both nanorutile TiO_2 and cubic rocksalt

$LiTiO_2$, Figs. 6a and b display the 1st, 4^{th,} and 5th discharge-charge curves of TiO_2 when

discharge to 1.4 V and 1.0 V, respectively. Three representative points were selected for

use in ex situ XRD tests from the corresponding discharge-charge curves. Figs. 6c and d

show the XRD patterns at corresponding charged states after discharge to 1.4 and 1.0 V,

respectively. Fig. 6c confirms that TiO_2 nanosticks maintain a stable rutile structure upon

successive Li-ion insertion/de-insertion processes when the lower cut-off voltage was limited to 1.4 V. However, when further discharged to 1.0 V, the electroactive c-LiTiO$_2$ phase formed after the irreversible phase transformation during the first discharge seems to maintain a stable and reversible structure upon cycling (Fig. 6d). The maximum expansion observed in the first cycles is 2% (Table S4 of SI) indicative of an excellent structural reversibility upon Li$^+$ insertion and extraction in disordered rocksalt c-LiTiO$_2$, in tune with the excellent electrochemical reversibility. The voltage profile of first charge (Fig. 6b) and ex situ XRD clearly indicate that the formation of c-LiTiO$_2$ at the equilibrium potential of 1.2 V (Fig 4a) upon first discharge is irreversible. Therefore, the claimed good performance of nanorutile as an anode material is a misnomer, as the high-performance material is the disordered nanosized rock salt type c-LiTiO$_2$.

The S-shaped voltage profile upon lithium extraction and further insertion in c-LiTiO$_2$ observed in Fig. 6b points to a reversible process through a single-phase domain. A cell cycled four times at C/20 was further discharged under PITT mode to observe the current relaxation. The typical behaviour is represented in Fig. S11 of SI. The observed current relaxation, approaching a t$^{-1/2}$ power law, confirms the mechanism to be the formation of a solid solution. Upon galvanostatic cycling it involves ca. 0.7 Li/f.u (Fig 3a) and develops a fair reversible capacity (ca. 180 mAh g^{-1}) that is kept for long cycling (Fig 3b and Fig. S3b of SI) corresponding to ~0.55 Li/f.u in agreement with previous reports (see for instance [4, 13, 37, 38] and other references in Table S1 of SI). The amount of lithium that can be cycled points to a wide solid solution range Li$_{0.3}$TiO$_2$-LiTiO$_2$.
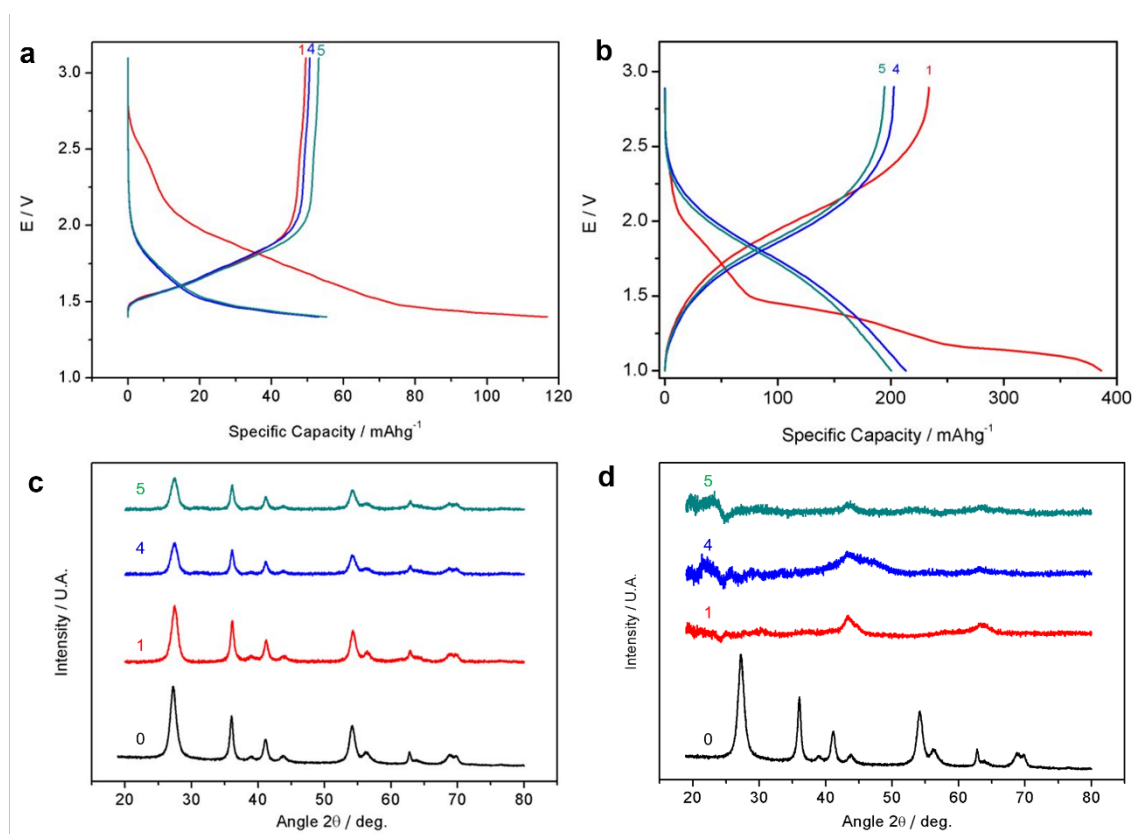
Figure 6: 1st, 4th, and 5th discharge-charge curves of rutile TiO_2 nanosticks in the **a)** 3.0-1.4 V and **b)** 3.0-1.0 V range. Corresponding ex situ XRD patterns at charged states after cycling in the **c)** 3.0-1.4 V and **d)** 3.0-1.0 V range.

3.3. The nature of the discharged nanorutile: c-LiTiO₂

With the knowledge obtained through the PITT analysis and ex situ XRD, we can now return to debate the structure of the fully discharged $LiTiO_2$, which is achieved through a two-phase transformation beyond ~0.63 Li as deduced from PITT. Although

the fully lithiated phase has low crystallinity, and only a few broad Bragg reflections are generally observed [4, 13, 17, 29], diffraction data has allowed for indexing, and a *Fm-3m* rock salt structure, a *R-3m* hexagonal structure, and a closely related *P2/m* monoclinic structure have been suggested.

In the rock salt structure, the Li and Ti cations are randomly distributed on the octahedral sites in the cubic close packed (ccp) oxygen lattice (Fig. 7c), while in the latter two structures, the cations are ordered within the ccp oxygen lattice in such a way that alternating Ti- and Li-layers are formed (Figs. 7a and b). The disordered cubic NaCl structure with a = 4.140 Å [39, 40] has been prepared by reaction of the corresponding binary oxides at 1000ºC or, more recently, mechanochemically [13] by milling lithium metal and TiO_2 rutile at room temperature, both under argon atmosphere. Hexagonal $LiTiO_2$, synthesized by Hewston *et al.* [41] for the first time, crystallises in the α-$NaFeO_2$-type structure, with cell parameters a = b = 2.881 Å and c = 14.602 Å (Fig. 7a). The space group is *R-3m* as for other first-row ternary $LiMO_2$ oxides (M = V, Cr, Co, Ni). Macklin *et al.* [36] ascribed a phase with composition $Li_{0.8}TiO_2$, obtained from a lithium polymer electrolyte cell discharged at 120ºC, to hexagonal $LiTiO_2$ based on ex situ XRD. Later, Hu *et al.* [4] obtained the composition $Li_{0.8}TiO_2$ in nanometer-sized rutile TiO_2 taken from a cell discharged to 1 V vs. Li^+/Li. The corresponding SAED pattern could be indexed as hexagonal $LiTiO_2$, and the diffraction peaks in the XRD pattern detected at 2θ of 43.56° (d = 2.06 Å) and 63.57° (1.46 Å) were ascribed, respectively, to the 104 and 0010 Bragg peaks of hexagonal $LiTiO_2$. It must be noted that the 0010 reflection is forbidden in trigonal space group *R-3m* and hence, the spacing of 1.46 Å is correctly ascribed to the 10-8 reflection.

The *P2/m* structure is simply a monoclinic distortion of the hexagonal structure and is thus often denoted *P2/m*$_{HEX}$ (not to be confused with *P2/m*$_{RUT}$). The *P2/m*$_{HEX}$ structural model has been confirmed both by powder neutron diffraction and first-principle calculations [29, 42]. The neutron diffraction pattern of the highly lithiated compound $Li_{0.85}TiO_2$ was modelled with the monoclinic space group *P2/m*, and lattice parameters were given as a = 5.078 Å, b = 2.951 Å, c = 5.022 Å, β = 71.7°, α = γ = 90°.

It must be pointed out here that it is not possible to distinguish between cubic and hexagonal $LiTiO_2$ based only on the two diffraction maxima corresponding to spacings of 2.06 Å and 1.46 Å, as done by several authors [4, 36]. The 2.06 Å and 1.46 Å spacings are indistinctively indexed, respectively, with 200_{Fm-3m}, 220_{Fm-3m} or 104_{R-3m}, $10-8_{R-3m}$. Although the low crystallinity of this phase complicates analysis of the diffraction data, only hexagonal $LiTiO_2$ presents the characteristic 003 Bragg peak at a much lower 2θ angle of 18.42° (spacing d = 4.87 Å) and is absent in cubic $LiTiO_2$. Interestingly, neither in Macklin's [36] nor Hu's work [4] is there any evidence for the presence of the hexagonal 003 reflection. To gain insight into this exciting question, we performed Rietveld refinements using ex situ XRD data (Fig. 7) of our nanosized TiO_2 rutile from a cell at first charge to 3 V after a full discharge-charge cycle in the 3.0 - 1.0 V range. Diffraction profiles were modelled with the *R-3m* hexagonal structure (Fig. 7a), the closely related *P2/m* monoclinic structure (Fig. 7b), and *Fm-3m* rock salt structure (Fig. 7c).

It is evident from Fig. 7 that structural refinement of c-Li$_x$TiO$_2$ was only successful in the cubic space group *Fm-3m*. Refined lattice parameters were a = b = c = 4.128(1) Å, V = 70.33(4) Å^3. Final agreement indices of refinement were: R$_{wp}$ = 4.20%, R$_p$ = 3.26% and R$_{Bragg}$ = 2.5%. Thus, our study proves that electrochemical insertion of

lithium into nanorutile TiO_2 down to 1 V produces $LiTiO_2$ with a rock-salt type structure,

in which Li and Ti atoms are disordered on the same 4b site. No reasonable refinements

were achieved with the other structure models (Figs. 7a and b).
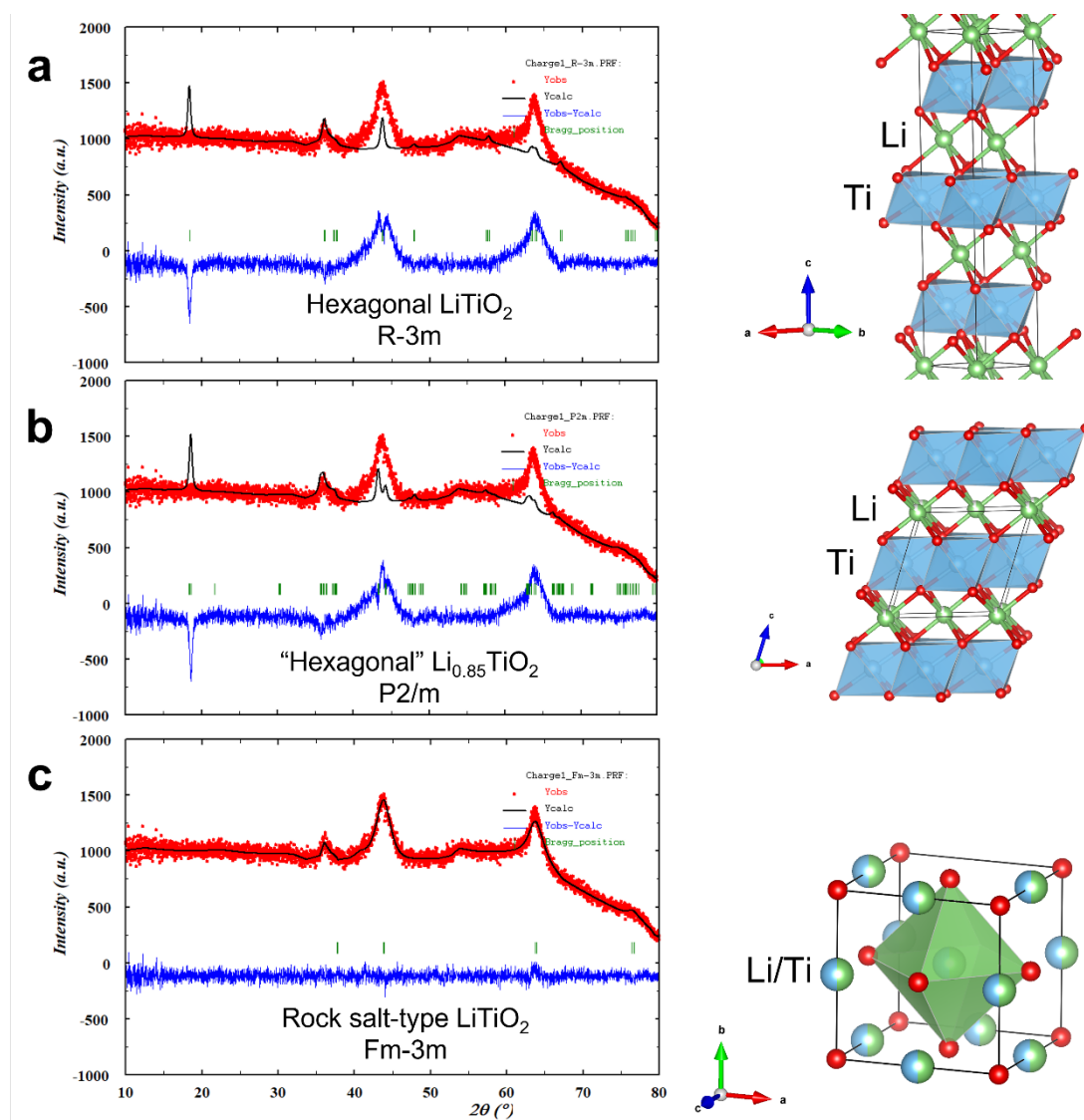
Figure 7: (left) The Rietveld refinement from *ex situ* X-ray diffraction data of a rutile

TiO_2 electrode at charge to 3.0 V, 1st cycle. Experimental (red points), calculated (solid

black line) and their difference (blue line at bottom of each XRD); (right) Structural

models used were: **a)** trigonal $LiTiO_2$ (S.G. *R-3m*, hexagonal setting); **b)** "hexagonal"

$Li_{0.85}TiO_2$ (S.G. *P2/m*) and **c)** cubic $LiTiO_2$ (S.G. *Fm-3m*, disordered rock-salt-type). Li: green spheres, Ti: blue spheres, O: red spheres.

3.4. An insight into the electrochemical performance of c-LiTiO₂

Lithiation of nanorutile TiO_2 produces c-$LiTiO_2$ that behaves afterwards as a high-performance anode material. Therefore, the cycling performance of nanorutile TiO_2 in the 3.0-1 V range, extensively reported in the literature (see for instance Table S1 of SI), is due to c-$LiTiO_2$ rather than TiO_2 itself. Table S1 of SI shows that cyclability and capacity is strongly dependent on the morphology of starting nanorutile, which also may influence that of c-$LiTiO_2$.

The relevant performance of the TiO_2 nanorutile herein presented is a reversible cycling of ~0.65-0.70 Li (240-260 mAh g^{-1}) after the first discharge, once it has been transformed to c-$LiTiO_2$, afterwards showing excellent capacity retention at high current rates. To gain further insights regarding whether electrochemical activity of c-$LiTiO_2$ involves fast lithium deinsertion/insertion into the cubic phase, or the observed capacity and reversibility is also due to interfacial charges, we determined lithium diffusion coefficients of c-Li_xTiO2 and further analysed the relative faradic/capacitive contributions.

A cell was previously cycled four times and finally left to reach equilibrium at the charged state (voltage equilibrium 2.455 V). Impedance was measured at this voltage and

at 2.2, 2.0 and 1.8 V along the 5th discharge, all of which belong to the solid solution region. These voltages were equilibrated in typical Potentiostatic Electrochemical Impedance Spectroscopy (PEIS). As an example, Fig. S12 of SI shows a Nyquist plot depicting the impedance response of c-Li$_x$TiO$_2$ at 2.2 V in a three-electrode cell. The typical spectrum should comprise the responses due to the impedance of lithium transport through the electrolyte (modelled by a resistance, R), charge transfer and double layer (modelled by a resistance in parallel to a constant phase element, R//CPE), passivation layer (also modelled with another R//CPE), and mass diffusion (a Warburg element, W). For our particular purpose we note the low frequency response due to lithium-ion diffusion into the bulk. The equivalent circuit shown in the inset of Fig. S12a was used for fitting the experimental data. Only one R//CPE element was used in the fitting because only one depleted semiarch is seen instead of the two expected ones. This is due to very close relaxation frequencies of the corresponding semicircles, which therefore overlap. Finally, an additional constant phase element, CPE, was used to consider the deviation of the spike from 45º. Warburg coefficient values, A_W, were read from the minimum of – Im(Z) $\omega^{1/2}$ versus ω plots (See Fig. S12b for a typical example for c-LiTiO$_2$ at 2.2 V). At this minimum, the Warburg diffusion process is the only contribution to EIS data. The *Aw* values obtained were afterwards used in the fitting of the Im(Z)-Re(z) impedance data confirming the model used and hence the presence of mass diffusion at the investigated voltages. Resulting lithium diffusion coefficients at the selected potentials are given in Table 1.

For the sake of comparison, the lithium diffusion coefficient in the rutile formed in region II was also determined. At 1.75 V, the estimated composition of rutile is Li$_{0.15}$TiO$_2$ belonging to the solid solution domain of region II, and the experimental D$_{Li+}$

is 6.25 x 10^{-15} cm^2 s^{-1}. When compared with theoretical calculations for $Li_{0.5}TiO_2$ [35] this value is nine orders of magnitude lower than the one expected along the c-direction, and of the same order of magnitude as D_{Li+} in the *ab-* plane. This difference can be related to the impediment of 1 D diffusion due to immobile point defects. It has been reported that the presence of point defects in 1 D diffusion makes the diffusion coefficient size dependent. It is expected that the higher diffusivity at the nanoscale is not sustained in large crystals [21]. In our case the diffusion path follows the *c*-direction which result to be the longest dimension of the crystals (5 nm in width and ≥50 nm in length). Some other authors [43-45] also found experimental D_{Li+} (~ 10^{-9} - 10^{-13} cm^2 s^{-1}) much lower than the theoretical one.

Table 1 shows that lithium diffusion in the disordered rock salt c-Li_xTiO_2 is also not very favourable, as D_{Li+} is very low as well, in the order of 10^{-16} – 10^{-15} cm^2 s^{-1}. Interestingly, the low diffusion coefficient of c-Li_xTiO_2 anticipates a poor power rate but data here, presented in Fig S3 of SI, and those reported by many authors (Table S1 of SI and references included there) indicate that high capacity is developed at high current despite the poor kinetics of lithium diffusion in c-Li_xTiO_2.

Table 1: Lithium diffusion coefficient of nanorutile TiO_2 (1st discharge) and c-$LiTiO_2$ (5th discharge) at different voltages.

Discharge	E / V	phase	$D_{(Li+)}/$ cm^2 s^{-1}
1st	1.75	Rutile (phase II)	6.25 x 10^{-15}
5th	2.45 (OCV)	cubic rock salt	1.7 x 10^{-16}
5th	2.2	cubic rock salt	5.4 x 10^{-16}
5th	2	cubic rock salt	1.0 x 10^{-15}

5th	1.8	cubic rock salt	2.6×10^{-15}

Considering the low values of D_{Li+}, a significant role of capacitive processes cannot be discarded to understand the good power rate. Recently, the important role of surface storage mechanism in several titanium oxide polymorphs including amorphous TiO_2 have been suggested based on DFT calculations [46]. In the present work, capacitive and faradic contributions to the total capacity at different current rates have been determined using the relationship between current intensity and sweep rate, $i = av^b$ [47]. Parameter b equals 1 in the case of capacitive processes whereas it equals 0.5 for diffusion-controlled processes [48], as is the case of the faradic processes corresponding to intercalation via electron transfer. As an example, Fig. S13 of SI shows the linear dependence of log v vs log i for cathodic and anodic sweeps of cyclic voltammogram at some selected potentials. The corresponding obtained slope, b, at each potential is indicated. The current response at a given potential is contributed by the two mechanisms according to: $i (V) = a_1v + a_2v^{1/2}$. By determining a_1 and a_2 both contributions can be separated and its change in the whole voltage range determined. Some recent examples of calculation procedure can be found in references [49, 50].

Two identical cells were first cycled once at the slowest scan rate of 0.009 mV s^{-1} to complete the irreversible transformation to c-LiTiO$_2$. Afterwards, one cell was scanned at slow rates and the other at very fast rates. Fig. 8a and 8b illustrates two voltammograms, conducted at very slow rate (0.009 mV s^{-1}) and at very fast rate (1.5 mV s^{-1}) respectively. Considering that the black contour represents the total current at each voltage while the red contour, enclosing the shaded area, represents the capacitive

contribution at each voltage, it turns out that the difference between both areas is related

to the faradic contribution. Fig. 8 shows a bar plot illustrating the variation of both

contributions to total capacity at different rates. It clearly shows that the capacitive

contribution is very significant at any scan rate. The faster the scan rate the higher the

capacitive contribution. At 0.3 mV s^{-1} and higher sweep rates, it accounts for more than

50% of total specific capacity, and the capacitive contribution is ca. 90% at 1.5 mV s^{-1}.

This demonstrates that the good rate performance of c-LiTiO$_2$ is mainly due to surface

physicochemical processes, most likely redox pseudocapacitive and double layer. The

variety of capacities found for nanorutiles in the literature (see or instance Table S1 of SI

and references therein cited) is therefore explained as due to the very different

morphologies and hence, surface areas, that contributes differently to the total capacity.
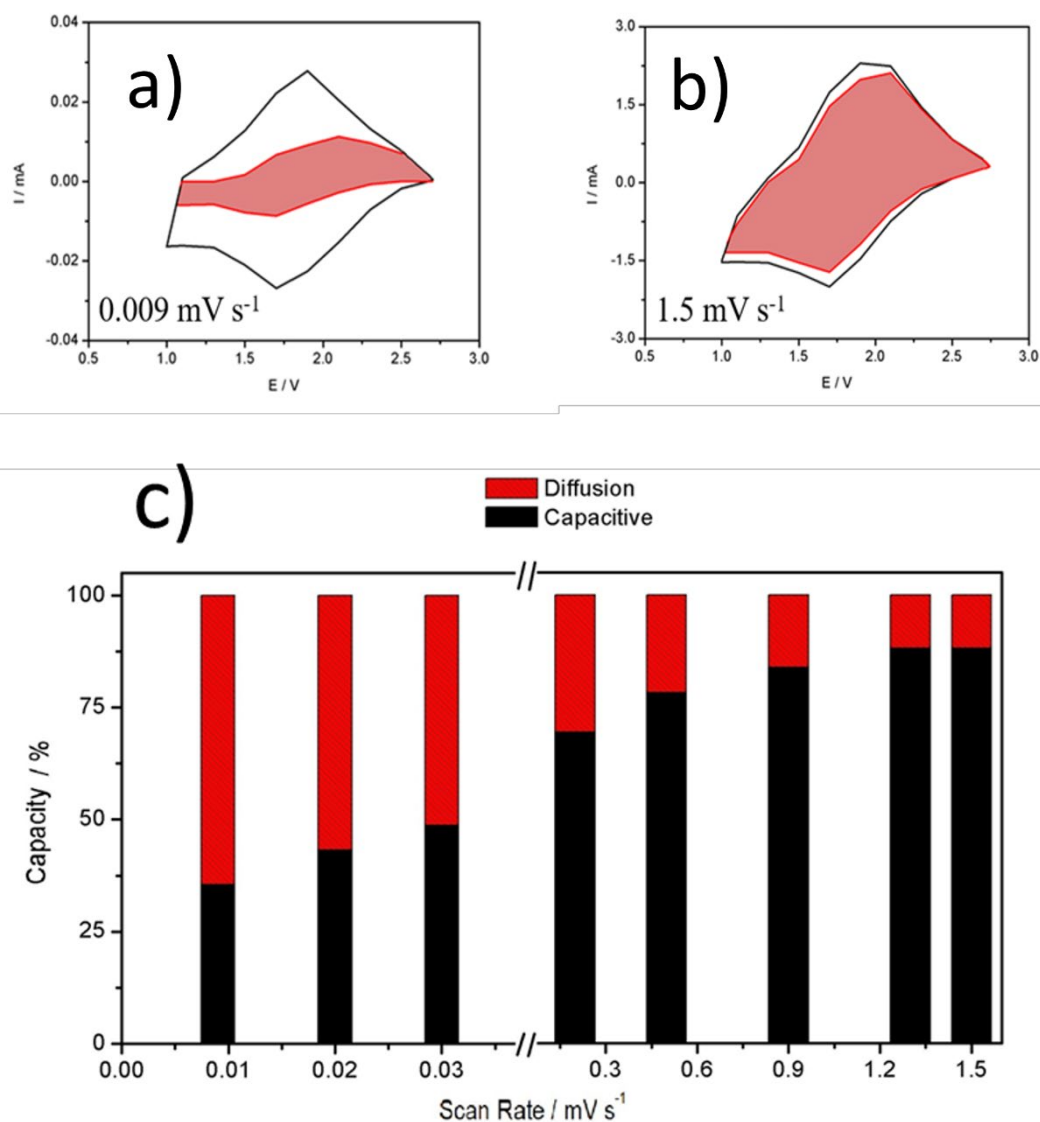
Figure 8: Cyclic voltammograms at: **a)** 0.009 mV s^{-1}; **b)** 1.5mV s^{-1} sweep rates and respective capacitive contributions (area inside the red contour area) to total capacity (area inside the black contour).   **c)** Bar chart showing the contribution (%) of capacitive and faradic processes to total capacity of c-LiTiO$_2$ as a function of the scan rate.

4. Conclusions

Rutile TiO_2 with nanostick morphology (~5 nm in width and ≥50 nm in length) has been prepared following a new synthetic path using a cost-effective two-step process, which involves ceramic synthesis of hollandite $K_{0.2}TiO_2$ precursor with subsequent oxidation in strong acidic media. As-prepared TiO_2 exhibits high electrochemical performance typical of nanosized rutile: i) a first disch9arge (above 385 mAh g^{-1}) that clearly exceeds 1 Li/f.u. (336 mAh g^{-1}) required to red9uce Ti^{4+} to Ti^{3+}, ii) a different voltage profile of first discharge and following ones; iii) an excellent power rate.

A closer examination of the first discharge using PITT measurements carried out under thermodynamic equilibrium conditions unveiled a complete Li-TiO_2 phase diagram. It reveals a non-faradic contribution to the excess of capacity at high voltage, 3-2.25 V, and two rutile solid solutions at lower voltages, 2.25-1.2 V, separated by a two-phase region. Lithium insertion is reversible in the rutile solid solution.

The lower voltage region below 1.2 V shows a biphasic reaction upon which quasi-stoichiometric cubic $LiTiO_2$ with a disordered rock-salt type structure appears. This cubic structure is stable upon lithium insertion/de-insertion with outstanding capacity retention, owing to little changes in the cell volume upon cycling. Our findings regarding the cubic symmetry of discharged nanorutile TiO_2, and hence Li/Ti disordering, agrees with the result of Baudrin *et al.* [13] but disagrees with other previous reports that claimed Li and Ti are ordered in a layered hexagonal structure [4, 14, 36] . The main conclusion is that the term "high performance nanorutile TiO_2 anode material" is somewhat misleading, and we should consider cubic $LiTiO_2$ (c-$LiTiO_2$) as the true high-performance anode material.

Regarding the origin of its good performance, particularly, it shows that its good power rate behaviour is not due to fast lithium diffusion as, in fact, it is strongly inhibited ($D_{Li+} \approx 10^{-15}$ cm^2 s^{-1}), and most capacity arises from capacitive processes. At 0.3 mV s^{-1} and higher sweep rates it accounts for more than 50% of total specific capacity, and the capacitive contribution is ca. 90% at 1.5 mV s^{-1}. Even at the very slow rate of 0.009 mV s^{-1} the capacitive contribution is 50%.

CReditT authorship contribution statement

Flaviano García-Alvarado: Conceptualization, Supervision Methodology, Funding acquisition, Writing - original draft, Project administration, Resources. **Alois Kuhn**: Conceptualization, Methodology, Investigation, Writing –review & editing. **Pilar Díaz-Carrasco**: Methodology, Investigation, Validation. **Angélica Duarte**: Investigation, Formal analysis, Validation

Acknowledgements

Appendix A. Supplementary data

Supplementary data to this article can be found online at https://doi.org/xxxxxxxxxxx.

References

[1] T. Ohzuku, T. Kodama, T. Hirai, J. Power Sources, 14 (1985) 153-166.

[2] D.W. Murphy, F.J. Di Salvo, J.N. Carides, J.V. Waszczak, Materials Research Bulletin, 13 (1978) 1395-1402.

[3] T. Ohzuku, Z. Takehara, S. Yoshizawa, Electrochimica Acta, 24 (1979) 219-222.

[4] Y.-S. Hu, L. Kienle, Y.-G. Guo, J. Maier, Advanced Materials, 18 (2006) 1421-1426.

[5] M.T. Gutierrez-Florez, A. Kuhn, F. Garcia-Alvarado, International Journal of Inorganic Materials, 1 (1999) 117-121.

[6] A. Kuhn, R. Amandi, F. García-Alvarado, J. Power Sources, 92 (2001) 221-227.

[7] M.A. Reddy, V. Pralong, U.V. Varadaraju, B. Raveau, Electrochemical and Solid State Letters, 11 (2008) A132-A134.

[8] A.R. Armstrong, G. Armstrong, J. Canales, R. Garcia, P.G. Bruce, Advanced Materials, 17 (2005) 862-+.

[9] M.B. Vazquez-Santos, P. Tartaj, E. Morales, J.M. Amarilla, The Chemical Record, 18 (2018) 1178-1191.

[10] S. Lou, Y. Zhao, J. Wang, G. Yin, C. Du, X. Sun, Small, 15 (2019) 1904740.

[11] O.W. Johnson, Physical Review a-General Physics, 136 (1964) A284-&.

[12] D. Deng, M.G. Kim, J.Y. Lee, J. Cho, Energy & Environmental Science, 2 (2009) 818-837.

[13] E. Baudrin, S. Cassaignon, M. Koelsch, J.P. Jolivet, L. Dupont, J.M. Tarascon, Electrochemistry Communications, 9 (2007) 337-342.

[14] M.A. Reddy, M.S. Kishore, V. Pralong, V. Caignaert, U.V. Varadaraju, B. Raveau, Electrochemistry Communications, 8 (2006) 1299-1303.

[15] C. Jiang, I. Honma, T. Kudo, H. Zhou, Electrochemical and Solid State Letters, 10 (2007) A127-A129.

[16] C.K. Christensen, M.A.H. Mamakhel, A.R. Balakrishna, B.B. Iversen, Y.-M. Chiang, D.B. Ravnsbæk, Nanoscale, 11 (2019) 12347-12357.

[17] M. Vijayakumar, S. Kerisit, C. Wang, Z. Nie, K.M. Rosso, Z. Yang, G. Graff, J. Liu, J. Hu, The Journal of Physical Chemistry C, 113 (2009) 14567-14574.

[18] H. Usui, Y. Domi, S. Ohnishi, N. Takamori, S.-i. Izaki, N. Morimoto, K. Yamanaka, K. Kobayashi, H. Sakaguchi, ACS Materials Letters, 3 (2021) 372-378.

[19] D. Imazeki, C.C. van Gils, K. Nishio, R. Shimizu, T. Hitosugi, ACS Applied Energy Materials, 3 (2020) 8338-8343.

[20] D. McNulty, E. Carroll, C. O'Dwyer, Advanced Energy Materials, 7 (2017) 1602291.

[21] R. Malik, D. Burch, M. Bazant, G. Ceder, Nano Letters, 10 (2010) 4123-4127.

[22] M. Watanabe, Y. Komatsu, T. Sasaki, Y. Fujiki, Journal of Solid State Chemistry, 92 (1991) 80-87.

[23] J. Rodríguez-Carvajal, Physica B: Condensed Matter, 192 (1993) 55-69.

[24] W. Weppner, R.A. Huggins, Journal of The Electrochemical Society, 124 (1977) 1569-1578.

[25] C. Ho, I.D. Raistrick, R.A. Huggins, Journal of the Electrochemical Society, 127 (1980) 343-350.

[26] B. Fu, Z. Wu, S. Cao, K. Guo, L. Piao, Nanoscale, 12 (2020) 4895-4902.

[27] M. Latroche, L. Brohan, R. Marchand, M. Tournoux, Journal of Solid State Chemistry, 81 (1989) 78-82.

[28] J.C. Pérez-Flores, C. Baehtz, A. Kuhn, F. García-Alvarado, Journal of Materials Chemistry A, 2 (2014) 1825-1833.

[29] W.J.H. Borghols, M. Wagemaker, U. Lafont, E.M. Kelder, F.M. Mulder, Chemistry of Materials, 20 (2008) 2949-2955.

[30] A. Mamalchel, C. Tyrsted, E.D. Bojesen, P. Hald, B.B. Iversen, Cryst. Growth Des., 13 (2013) 4730-4734.

[31] Y.P. Chabre, Journal of The Electrochemical Society, 138 (1991) 329-330.

[32] M. Pfanzelt, P. Kubiak, S. Jacke, L. Dimesso, W. Jaegermann, M. Wohlfahrt-Mehrens, Journal of The Electrochemical Society, 159 (2012) A809-A814.

[33] S. Sarciaux, A.L. La Salle, A. Verbaere, Y. Piffard, D. Guyomard, J. Power Sources, 81 (1999) 661-665.

[34] Y. Chabre, Electrochemical Spectroscopy and In-Situ Diffraction Studies of Intercalation Compounds, in: P. Bernier, J.E. Fischer, S. Roth, S.A. Solin (Eds.) Chemical Physics of Intercalation II, Springer US, Boston, MA, 1993, pp. 181-192.

[35] M.V. Koudriachova, N.M. Harrison, S.W. de Leeuw, Solid State Ionics, 157 (2003) 35-38.

[36] W.J. Macklin, R.J. Neat, Solid State Ionics, 53-56 (1992) 694-700.

[37] P. Kubiak, M. Pfanzelt, J. Geserick, U. Hörmann, N. Hüsing, U. Kaiser, M. Wohlfahrt-Mehrens, J. Power Sources, 194 (2009) 1099-1104.

[38] J.S. Chen, X.W. Lou, J. Power Sources, 195 (2010) 2905-2908.

[39] A. Lecerf, Comptes Rendus Hebdomadaires Des Seances De L Academie Des Sciences, 254 (1962) 2003-2004.

[40] A. Lecerf, Annales De Chimie France, 7 (1962) 513-515.

[41] T.A. Hewston, B.L. Chamberland, Journal of Physics and Chemistry of Solids, 48 (1987) 97-108.

[42] M.V. Koudriachova, N.M. Harrison, S.W. de Leeuw, Solid State Ionics, 175 (2004) 829-834.

[43] A.V. Churikov, V.A. Zobenkova, K.I. Pridatko, Russian Journal of Electrochemistry, 40 (2004) 63-68.

[44] K. Kanamura, K. Yuasa, Z. Takehara, J. Power Sources, 20 (1987) 127-134.

[45] S. Bach, J.P. Pereira-Ramos, P. Willman, Electrochimica Acta, 55 (2010) 4952-4959.

[46] J.A. Yuwono, P. Burr, C. Galvin, A. Lennon, ACS Applied Materials & Interfaces, 13 (2021) 1791-1806.

[47] H. Lindström, S. Södergren, A. Solbrand, H. Rensmo, J. Hjelm, A. Hagfeldt, S.-E. Lindquist, The Journal of Physical Chemistry B, 101 (1997) 7717-7722.

[48] J. Wang, J. Polleux, J. Lim, B. Dunn, The Journal of Physical Chemistry C, 111 (2007) 14925-14931.

[49] M. Sathiya, A.S. Prakash, K. Ramesha, J.M. Tarascon, A.K. Shukla, Journal of the American Chemical Society, 133 (2011) 16291-16299.

[50] S. Rubio, R.R. Maça, M.J. Aragón, M. Cabello, M. Castillo-Rodríguez, P. Lavela, J.L. Tirado, V. Etacheri, G.F. Ortiz, J. Power Sources, 432 (2019) 82-91.